

Trap States Ruling Photoconductive Gain in Tissue-Equivalent, Printed Organic X-Ray Detectors

Ilaria Fratelli, Laura Basiricò, Andrea Ciavatti, Zachary A. Lamport, John E. Anthony, Ioannis Kymissis, and Beatrice Fraboni*

Organic semiconductors are excellent candidates for X-ray detectors that can adapt to new applications, with unique properties including mechanical flexibility and the ability to cover large surfaces. Their chemical composition, primarily carbon and hydrogen, makes them human tissue equivalent in terms of radiation absorption. This is a highly desirable property for a radiation dosimeter to be employed in medical diagnostics and therapy, however a low-Z composition limits the absorption of ionizing radiation. The detection efficiency can be enhanced by considering the photoconductive gain (PG) effect, a significant contributor to the ionizing radiation detection mechanism in this class of materials. In this work, a process of controlled solution deposition by nozzle printing and crystallization of an organic semiconductor thin film is demonstrated whereby a flexible, arrayed thin-film X-ray detector with record X-ray sensitivities among flexible radiation detectors ($S = (9.0 \pm 0.4) \times 10^7 \mu\text{C Gy}^{-1} \text{cm}^{-2}$) is developed. The excitonic peaks responsible for the activation of the PG effect are investigated and identified using a novel technique called photocurrent spectroscopy optical quenching, and the analysis of the changes in trap states is further demonstrated.

emerging applications, including radiation-based therapies and diagnostic techniques. In the last decade, organic semiconductors have emerged as excellent candidates for a new class of ionizing radiation detectors able to meet the challenge of these requirements.^[1–3] The possibility to deposit them from solution and at low temperatures allows for device fabrication employing low-cost processes onto polymeric flexible substrates, yielding pixelated architectures which can easily be scaled onto large areas. Organic materials offer a unique and fundamental property for medical radiation dosimetry (e.g., radiotherapy^[4] and proton-therapy^[5]): their low atomic numbers and density make them human tissue equivalent in terms of energy absorption from ionizing radiation. Mimicking human tissues offers two important advantages compared to inorganic materials: i) avoiding complex calibration procedures and ii)

offering the possibility to place the dosimeter between the radiation source and the patient without interfering with the radiation beam.

A disadvantage of the low atomic number of organic materials is that this results in poor absorption of ionizing radiation, and thus low external quantum efficiency. To tackle this issue, several strategies have been proposed in the literature, one of which involves blending the organic semiconductors and polymers with high-Z nanocomposites, leading to an increase of the attenuated fraction of the device.^[6–8] Another very effective strategy relies on careful tuning of the photoconductive gain (PG) effect. This effect is mediated by electrically active trap states which induce an inner amplification of the photocurrent generated by the absorption of high energy photons. Thus, an insightful study of the electrically active trap states, both for minority and majority carriers, in organic thin-film-based devices would allow tuning of the PG to boost the sensitivity of the detectors.

Traps in organic semiconductors have a deep impact on the performance of electronic devices and can be described as a variety of electronic states at grain boundaries, interfaces, and defects. These trap states do not present discrete, sharp energy levels, rather they exhibit broad Gaussian-like or exponential distributions. For these reasons, their control and characterization is still not trivial.^[9] An effective control of trap states in organic materials is even more difficult when scaling up the size of the substrates due to the poorer control of the interfaces as well as the crystallization dynamics of the semiconducting layer. In this work, we fabricated organic field-effect transistors

1. Introduction

Novel radiation detectors that possess both mechanical flexibility and the ability to cover a large area are an urgent need in

I. Fratelli, L. Basiricò, A. Ciavatti, B. Fraboni
Department of Physics and Astronomy
University of Bologna

Viale Berti Pichat 6/2, Bologna 40127, Italy
E-mail: beatrice.fraboni@unibo.it

I. Fratelli, L. Basiricò, A. Ciavatti, B. Fraboni
Institute of Nuclear Physics
INFN-BO

Viale Berti Pichat 6/2, Bologna 40127, Italy

Z. A. Lamport, I. Kymissis
Department of Electrical Engineering
Columbia University
New York, NY 10027, USA

J. E. Anthony
Center for Applied Energy Research
University of Kentucky
Lexington, KY 40511, USA

 The ORCID identification number(s) for the author(s) of this article can be found under <https://doi.org/10.1002/admt.202200769>.

© 2022 The Authors. Advanced Materials Technologies published by Wiley-VCH GmbH. This is an open access article under the terms of the Creative Commons Attribution-NonCommercial License, which permits use, distribution and reproduction in any medium, provided the original work is properly cited and is not used for commercial purposes.

DOI: 10.1002/admt.202200769

(OFETs) by depositing the active layer from solution through a low-temperature and low-cost fabrication printing technique called pneumatic nozzle printing (PNP),^[10] which allows the fabrication of fully flexible devices, semiconductor patterning, and large-area scalability. PNP combines the advantages of standard printing techniques^[11] (e.g., patterning the semiconducting layer) with those of meniscus shearing techniques^[12] (e.g., offering excellent control of the growth and crystallization of the organic material). This technique allowed us to deposit organic thin films of TIPS-Pn (6,13-bis(triisopropylsilylethynyl)pentacene) and TIPG-Pn (analogous molecule where the two Si atoms have been substituted with two Ge atoms) in uniform, well-packed, and aligned microcrystalline structures. We fabricated flexible, arrayed, thin-film X-ray detectors with record X-ray sensitivities among flexible radiation detectors up to $S = (9.0 \pm 0.4) \times 10^7 \mu\text{C Gy}^{-1} \text{cm}^{-3}$.

The printing procedure employed in this study permits tuning of the morphology and packing of the film, which in turn allows ones to selectively vary key features related to trap states that affect both the charge transport and collection and, ultimately, the detection mechanism. We investigate electrically active traps for minority carriers by photocurrent spectroscopy with optical quenching. This technique identifies the excitonic peaks which induce the inner amplification mechanism. As a result of the activation of the PG effect induced by the simultaneous presence of UV-vis and X-ray photons, we experimentally assessed for the first time the presence and the role of the electrically active traps for minority carriers responsible for this physical phenomenon. Through this experiment, we also evaluate the different efficacy of PG activation in TIPS-Pn and TIPG-Pn.

2. Results and Discussion

In this work, we developed flexible organic X-ray detectors, based on OFETs integrated in a pixelated configuration (2×6 pixels arrays with one common source and independent gate and drain electrodes, **Figure 1a**). The active layer is an organic semiconducting thin film deposited by PNP. This printing strategy allows the printhead to continuously draw out the organic ink, imposing a preferential direction to the crystallization while patterning the deposited layer by moving the nozzle in the 2D plane. We employed two different organic small molecules for this work: TIPS-Pn and the analogous molecule TIPG-Pn.^[13] **Figure 1b–d** reports optical images of TIPG-Pn thin films (TIPS-Pn is shown in **Figure S1** in the Supporting Information), showing their well-packed microcrystalline structures aligned along the printing direction. We measured the thickness of the microcrystals from atomic force microscope (AFM) images (**Figure 1e,f**) and it varies between 45 and 180 nm depending on the deposition parameters and on the molecules employed (see **Table T1**, Supporting Information). More details about the printing procedure are reported in the Experimental Section.

We implemented as-deposited TIPS-Pn and TIPG-Pn thin films as the semiconducting layer of bottom gate–bottom contact OFETs, fabricated onto a 125 μm thick polyethylene naphthalate (PEN) substrate, achieving fully flexible devices

(**Figure 1h**). All electrodes were patterned by common photolithography processes. The typical output and transfer characteristic curves and the electrical parameters of the fabricated OFETs are summarized in the Supporting Information (**Table T2** and **Figures S2** and **S3** in the Supporting Information). The electrical properties of these devices (i.e., electrical mobility, threshold voltage, ON/OFF ratio, subthreshold swing slope) are comparable to the state of the art for flexible OFETs.^[14] The good spatial uniformity achievable by PNP is demonstrated by the comparable electrical properties observed for the OFETs laying in the same array and fabricated following the same procedures (i.e., printing parameters for the organic semiconductor deposition) (see **Figure S2d**, Supporting Information). **Figure 1i** shows the excellent stability over time of the TIPS-Pn-based OFETs, as the transfer characteristic of the same OFET acquired after 12 and 15 months remains unchanged. For the TIPG-Pn-based devices, the effect of long-term storage under ambient conditions produces a slightly higher degradation showing a reduction in electrical mobility of about 30% after 15 months (**Figure S4**, Supporting Information).

By varying the deposition parameters (e.g., speed, temperature), it is possible to control the solution supersaturation rate and consequently to tune the organic polycrystalline films' crystallization and the morphology.^[15,16] **Figure 2a** presents optical images of TIPS-Pn layers printed at different deposition speeds (in the range 0.1–1 mm s^{-1}). For fast deposition speeds ($>0.6 \text{ mm s}^{-1}$), randomly oriented small crystallites are obtained. As discussed by Yang et al.,^[10] in this evaporation regime a high supersaturation rate is expected which leads to a quasi-amorphous film obtained by nucleation processes. At slow deposition speeds ($<0.2 \text{ mm s}^{-1}$), large crystals are obtained but are formed with isotropic orientations and include voids which lead to a less packed and nonuniform spatial distribution. At intermediate speeds (>0.2 and $<0.6 \text{ mm s}^{-1}$), a lower rate of supersaturation leads to the growth of long densely packed microcrystalline structures well-aligned along the printing direction. We achieved the same result with the TIPG-Pn molecules and the analogous images are reported in **Figure S1** in the Supporting Information. These differences in the crystallization of the organic semiconducting films strongly affect the transport properties of the material. **Figure 2b** shows the dependence of the charge carrier mobility extracted from OFETs based on TIPS-Pn and TIPG-Pn as a function of the deposition speed. These data are reported as the average value calculated over six OFETs fabricated with the same printing conditions. According to Yang et al.,^[10] the highest electrical mobility is recorded for organic layers deposited at intermediate speeds where, for both types of molecules, the long microcrystalline structures are aligned across the device channel and the film is spatially uniform and very well packed. When TIPS-Pn and TIPG-Pn are deposited at 0.6 and 0.2 mm s^{-1} , respectively, they form superior quality films providing the OFETs with the highest electrical mobility values, $\mu_{\text{TIPS}} = (0.10 \pm 0.02) \text{ cm}^2 \text{ V}^{-1} \text{ s}^{-1}$ for TIPS-Pn and $\mu_{\text{TIPG}} = (0.17 \pm 0.03) \text{ cm}^2 \text{ V}^{-1} \text{ s}^{-1}$ for TIPG-Pn. These values recorded for flexible devices fabricated onto polymeric substrates are one order of magnitude higher than for analogous OFETs where the TIPS-Pn was spin coated onto a rigid substrate (Si/SiO_2),^[10] confirming the high-quality films achievable by PNP. The brickwork packing motif of the

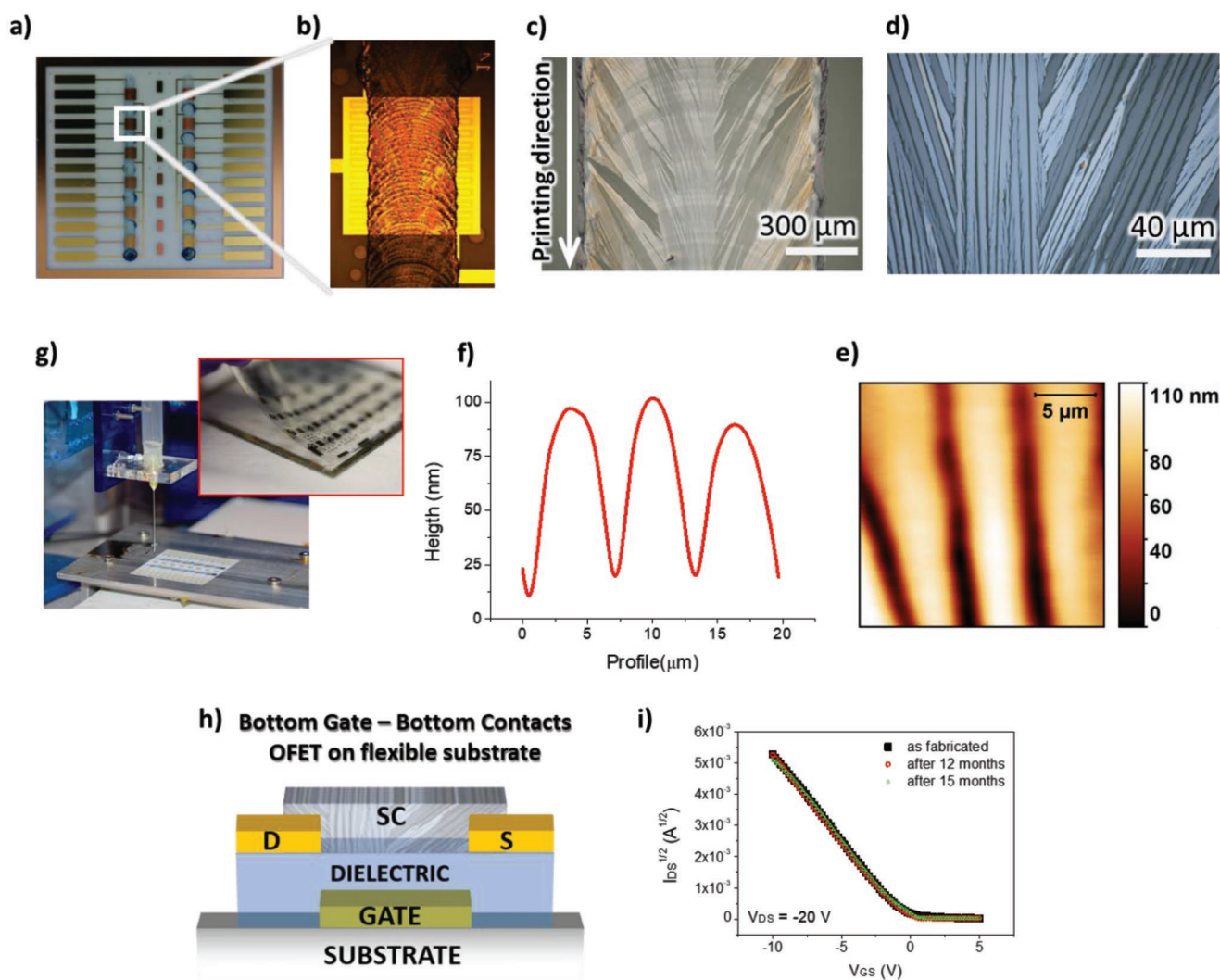


Figure 1. Organic semiconducting thin films deposited by PNP. Devices were fabricated onto a flexible, large area substrate. a) Layout of the samples where 12 OFETs are placed in two parallel arrays. The source electrode is in common for the pixels of the same array while the gate and the drain of each transistor are independent. b–d) Optical images of the TIPG-Pn semiconducting layer deposited by PNP. e) AFM image and f) microcrystalline profile. g) PNP setup. h) Bottom gate–bottom contact OFET architecture with printed organic film as active layer. i) Transfer characteristics in saturation regime acquired for a TIPS-Pn OFET deposited at 0.6 mm s^{-1} as soon as fabricated, after 12 and 15 months of shelf storage, demonstrating device stability.

pentacene conjugated core exhibited by both molecules provides similar transport properties (i.e., electrical mobility) for TIPS-Pn and TIPG-Pn films sharing similar morphologies.^[13]

We characterized our OFETs as direct X-ray detectors by testing them under a W-target X-ray tube (40 kVp and anodic current = 100–500 μA) at different dose rates (1.6–8.6 mGy s^{-1}). The entire area of the device is irradiated when the X-ray tube is turned on. Details about the X-ray tube calibration and dose rate measurements are reported in the Experimental Section. We assessed the detecting performance of the devices by monitoring the real-time I_{DS} photocurrent generated under X-ray irradiation (Figure 3a). We calculated the photocurrent measured for each dose rate as the difference between the I_{DS} flowing in the transistor channel when the sample is irradiated (i.e., at the end of the irradiation cycle) and the value of I_{DS} was recorded when the X-rays are turned off. All values are obtained as the average over three subsequent irradiation

cycles (i.e., 60 s X-ray on and 60 s X-ray off) at the same dose rate, as illustrated in the dynamic response curves (Figure 3a), which indicate a good reproducibility of the induced signal under the same irradiation conditions. We calculated the detectors' sensitivity for each device as the slope of the fitting curve reported in Figure 3b, normalized for the semiconducting active volume (i.e., $S_v = \frac{\partial \Delta I}{\partial DR} \frac{1}{V}$ where ΔI is the photocurrent, DR is the dose rate in air kerma, and V is the active volume) as described by Basiricò et al.^[17] The active volume of the OFETs is defined by the pixel area (4 mm^2) and the thicknesses of the semiconducting films (in the range 45–180 nm) that depend on the deposition conditions and are summarized in Table T1 in the Supporting Information. For the optimized deposition speed of 0.4 mm s^{-1} , we reached an average sensitivity of $S_{\text{TIPS}} = (6.0 \pm 3) \times 10^7 \mu\text{C Gy}^{-1} \text{ cm}^{-3}$ for TIPS-Pn-based detectors and $S_{\text{TIPG}} = (9.0 \pm 0.4) \times 10^7 \mu\text{C Gy}^{-1} \text{ cm}^{-3}$ with TIPG-Pn.

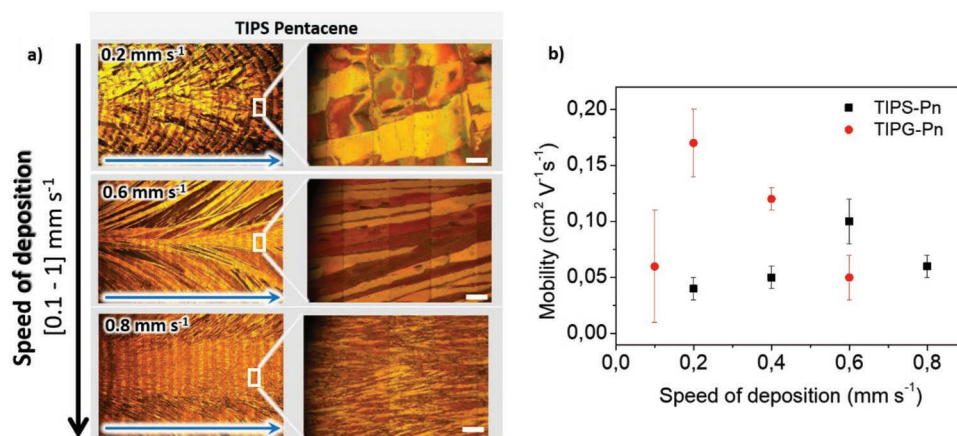


Figure 2. Control of morphology and transport properties. PNP allows full control of organic semiconductor crystallization by tuning the deposition parameters. a) Optical images showing varying crystallization of TIPS-Pn thin films deposited at different velocity ([0.2, 0.6, 0.8] mm s⁻¹). The blue arrows indicate the printing direction (white scale bar = 20 μm). b) Charge carrier mobility as a function of deposition speed.

Summaries of the sensitivity for all deposition speeds for both molecules are in Table T3 and Figure S5 in the Supporting Information. The excellent X-ray detection performance can be ascribed to the PNP deposition technique providing superior control of the microcrystalline alignment and molecular packing in the thin film, thus boosting the efficiency of organic thin-film detectors, as further detailed below.

It is noteworthy to recall that the detection of ionizing radiation in organic polycrystalline thin films is governed by a PG mechanism,^[17] mediated by electrically active trap states for minority carriers (here, electrons) which induces an inner amplification (G) of the primary photocurrent generated by the absorption of high energy photons (I_{CC}). The gain factor G can be expressed as the ratio between two characteristic times: τ_R which represents the recombination time of the trapped minority carriers and τ_T which is the transit time of the majority carriers through the channel length. Thus, in organic thin-film detectors, the photocurrent ΔI_{PG} can be expressed by the following equation, as obtained in refs. [17,18]

$$\Delta I_{PG} = G \times I_{CC} = \frac{\tau_R}{\tau_T} \times I_{CC} = \frac{\alpha}{\gamma} \times \left[\alpha \times \ln \left(\frac{\rho_0}{\rho_x} \right) \right]^{\frac{1-\gamma}{\gamma}} \times \frac{V \times \mu}{L^2} \times I_{CC} \quad (1)$$

where τ_R and τ_T have been expanded and in particular, α and γ describe the characteristic time-scale and the dispersion of trap states, ρ_0 and ρ_x are the material specific and radiation-induced carrier density, respectively, V is the applied bias, μ is the electrical mobility, and L is the transistor channel length. Thus, the total photocurrent ΔI_{PG} is the result of the combination of two different aspects of the detecting process: i) I_{CC} represents the ability of the active material to absorb radiation and collect the photoinduced charges, which is related to both the semiconductor composition and density, and the transport properties of the device; ii) the gain factor G which amplifies the I_{CC} and depends on the activation of the PG mechanism. In this work, we exploited all the parameters which determine the final photocurrent to maximize the efficiency of X-ray detection.

First, the use of transistors allowed a maximized ρ_0 by keeping the device in the saturation regime during the

irradiation ($V_{DS} = -20$ V; $V_{GS} = -5$ V). In fact, as reported in Figure S6 in the Supporting Information, the sensitivity obtained in the saturation regime is higher than the one in the linear regime because of the enhancement of majority carrier density in the transistor channel (ρ_0). The polarization of the gate electrode allows on/off switching of the transistor both as an electrical device and also as a detector (Figure S6, Supporting Information). This is a very desirable property for addressing pixels in a 2D-pixelated matrix.^[19]

Second, as demonstrated by Ciavatti et al.,^[20] by employing TIPG-Pn instead of TIPS-Pn the average atomic number of the detector active layer increases, enhancing the X-ray radiation absorption and thus the photocurrent I_{CC} generated by charge collection. This enhancement represents a great advantage offered by these specifically designed organic semiconducting molecules, directly imparting the desired properties to the bulk material and avoiding more cumbersome approaches such as blending with high-Z material nanostructures, which can affect the crystallization process and the transport properties of the electronic device. In the case of TIPG-Pn, the molecule was easily prepared by using germanyl-, rather than silyl-based acetylenes during the synthesis.^[21–24] Surprisingly, the bulk crystal structure of TIPG-Pn would not suggest utility in OFET applications, adopting an insulated edge-to-face arrangement in the solid state.^[13] Fortunately, the dominant thin-film polymorph of this compound adopts the same strongly π -stacked 2D “brickwork” arrangement seen for TIPS-Pn, thus allowing the films to adopt similar electronic characteristics to that well-known semiconductor.

Thanks to the control of crystallization parameters granted by PNP, it has been possible to enhance the PG effect, decreasing τ_T and increasing τ_R , thus reaching very high values for the factor G . The control over film crystallization and the well-packed and aligned microcrystalline structures provided by PNP aid in the production of high-performance transistors in terms of transport properties, reaching mobility values up to 0.2 cm² V⁻¹ s⁻¹, which decreases the τ_T . Further, this technique permitted tuning of the semiconducting film morphology to maximize the efficacy of minority carriers traps in increasing τ_R , critical to enhancing the PG as we recently reported.^[25]

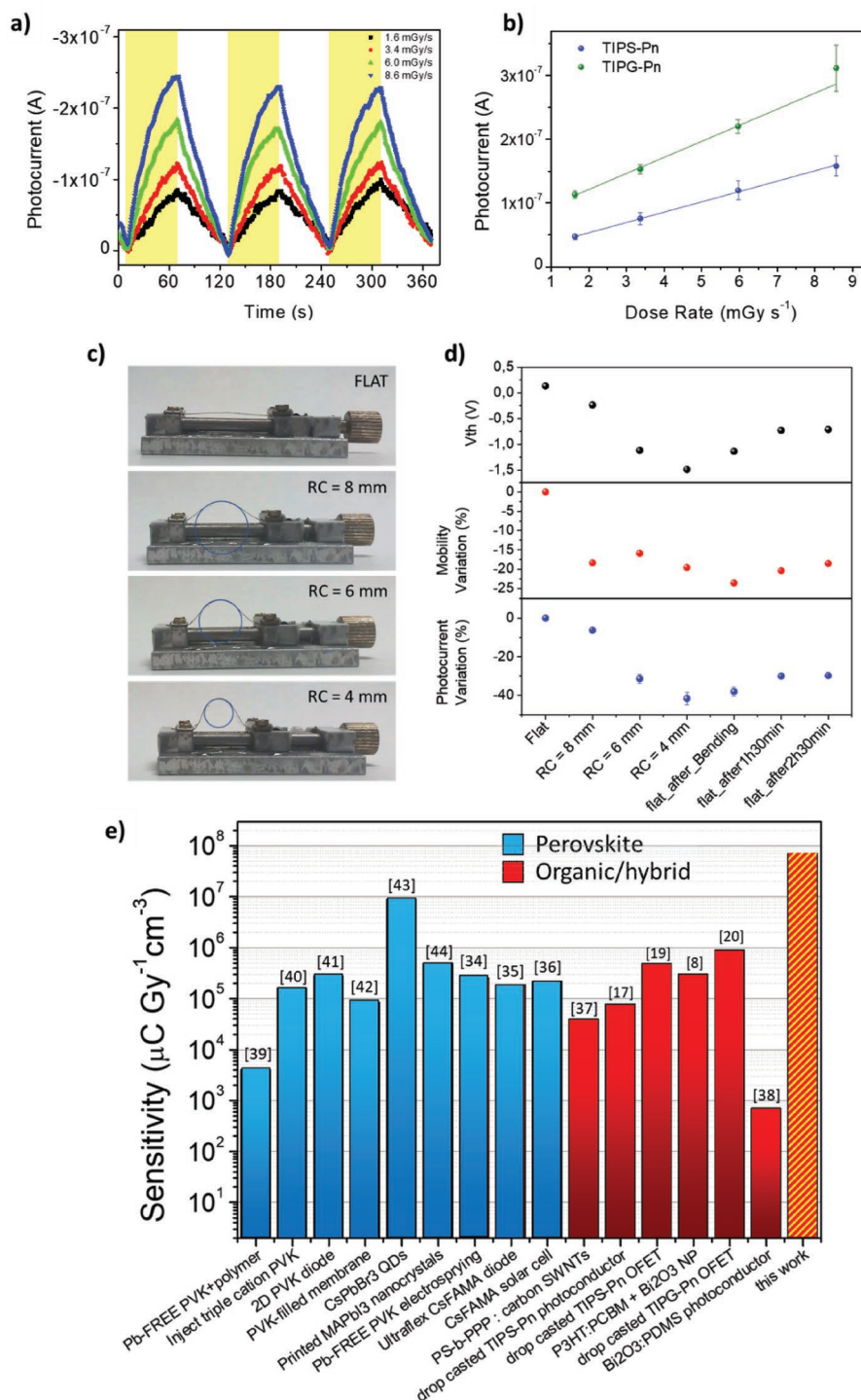


Figure 3. Printed OFETs as X-ray detectors. OFETs have been tested as X-ray detectors irradiating them under a W-target X-ray tube at 40 kV. a) Dynamic curve of the photocurrent induced by three subsequent irradiation cycles (60 s ON/60 s OFF) at four different dose rates (1.6–8.6) mGy s⁻¹. For each dose rate, three subsequent irradiation cycles are reported to demonstrate the reproducibility of the induced photocurrent. In this graph, the 0.4 mm s⁻¹ printed TIPG-Pn response is reported biased at V_{DS} = -20 V; V_{GS} = -5 V. b) Photocurrent as a function of the dose rates of radiation for TIPS-Pn (0.4 mm s⁻¹) and TIPG-Pn (0.4 mm s⁻¹) based devices. The sensitivity of the detector is the slope of the fitting curve. The mechanical flexibility of the detecting system has been evaluated. c) The device (TIPS-Pn-based OFET deposited at 0.4 mm s⁻¹) has been tested both electrically and under X-ray irradiation while flat and bent at three different curvature radii (RC = 8, 6, 4 mm). In each case, the transfer characteristics in saturation regime and the dynamic response of the detector have been acquired (Figure S7a,b, Supporting Information). The recovery of the sample was monitored for 2.5 h after the bending tests. d) The variation of the threshold voltage, electrical mobility, and X-ray photocurrent are reported for the different conditions, extrapolated from the graphs reported in Figure S7a,b in the Supporting Information. The electrical mobility of the OFETs decreases by about 20% at RC = 4 mm while the photocurrent degrades by about 40%. e) State of the art of flexible direct X-ray detector sensitivities (perovskite thin films in blue, organic semiconductor thin films in red).^[8,17,19,20,34–44]

Finally, the ability to exploit low-temperature processes allowed us to realize a fully flexible detector directly fabricated onto polymeric substrates. To assess the flex stability of our devices, we measured the transfer characteristics and the X-ray detection responses while the substrates were bent at radii (RC, Figure 3c) of 8, 6, and 4 mm. In Figure 3d, we report the data collected for a TIPS-Pn-based detector printed at 4 mm s⁻¹. The device was irradiated under the same conditions as the one reported in Figure 3a (40 kVp, 60 s ON/60 s OFF, 8.6 mGy s⁻¹, biased at V_{DS} = -20 V; V_{GS} = -5 V). The electrical parameters and the detection performance of the device are reported for different bending conditions (Figure 3d).

At a curvature radius RC = 4 mm, we observe a degradation of the X-ray photocurrent of about 40% which is in line with our previous results.^[17] The electrical mobility decreases of about 20% and the threshold voltage shifts of about 1.5 V toward negative values, due to the mechanical stress. After bending, the detector shows a slow recovery, indicating that the bending did not induce any permanent damage to the device.

The dynamic responses under X-ray irradiation, and the transfer characteristics acquired at different bending radii are reported in Figure S7a,b (Supporting Information). In Figure S7c,d in the Supporting Information, fatigue tests conducted on the same device are reported, confirming the performance of the devices under flex.

The combination of all these strategies resulted in highly sensitive flexible X-ray detectors. To the best of our knowledge, the sensitivity values achieved represent a record result for flexible direct X-ray detectors based on organic materials and even surpass perovskite-based films, as shown in Figure 3c. Other recent results with thin-film X-ray detectors based on organic small molecules, polymers, hybrid perovskites, tin mono-sulfide (SnS) nanosheets, both flexible and rigid are listed in Table T4 in the Supporting Information.^[26–33] It is important to note that such high sensitivities have been achieved upon irradiation of tens of seconds, which guarantees the full activation of the PG mechanism and the saturation of the effect. This mechanism of detection is based on the active trap states' characteristic lifetimes, leading to very long rise and fall times. Basiricò et al. demonstrated that shorter X-rays pulses (i.e., 100 ms)

can be reliably detected by these devices even if the photoinduced signal and the sensitivity are lower due to the partial activation of the amplification mechanism.^[3]

The record sensitivity shown in Figure 3 has been obtained with TIPG-based molecule. Tailoring a high-Z element in the molecular structure of the organic semiconductor is an effective strategy to boost the efficiency of the detector by increasing the absorption of ionizing radiation. In our previous work,^[20] we reported a sensitivity for the TIPG-Pn-based devices three times higher than that measured for the analogous TIPS-based detectors. But, considering the different attenuation fraction of the two molecules and the different thicknesses of the active layers, the difference between the two should be higher (i.e., $S_{\text{TIPG-Pn}} \approx 10 \times S_{\text{TIPS-Pn}}$). We ascribed the loss in TIPG-Pn performances to a smaller effective active area due to the lower area-coverage obtained for drop-casted TIPG-Pn films, with respect to TIPS-Pn ones. As reported here, PNP allows us to overcome this issue providing an excellent coverage for both types of organic molecules (Figure S1, Supporting Information). In Figure 4a, the optical images of two samples based on TIPS-Pn and TIPG-Pn deposited, respectively, at 0.6 and 0.4 mm s⁻¹ are reported. The films achieved using these deposition parameters show the same area coverage and similar morphology with comparable grain dimensions, shapes, and distributions. For these devices, which share similar morphologies and similar grain boundary density, the mean mobility values are comparable $\mu = (0.10 \pm 0.02) \text{ cm}^2 \text{ V}^{-1} \text{ s}^{-1}$ and $\mu = (0.12 \pm 0.01) \text{ cm}^2 \text{ V}^{-1} \text{ s}^{-1}$ for TIPS-Pn and TIPG-Pn, respectively. In Figure 4b, we compare the typical dynamic response of TIPS-Pn and TIPG-Pn under a 60 s irradiation cycle at different dose rates (in the range 1.6–8.6 mGy s⁻¹). From these curves, it is possible to calculate the sensitivity values reported in Table 1, showing how, also in our PNP deposited devices, the sensitivity of the TIPG-Pn devices is only three times higher than those measured for the TIPS-Pn devices. By considering the attenuated fraction of the two molecules (reported in Table 1 and extracted from the graph in Figure S8, Supporting Information), and the comparable transport properties (i.e., τ_T), morphologies, and area coverage, one should expect a more significant difference in performance between the two detectors. To better understand the cause of

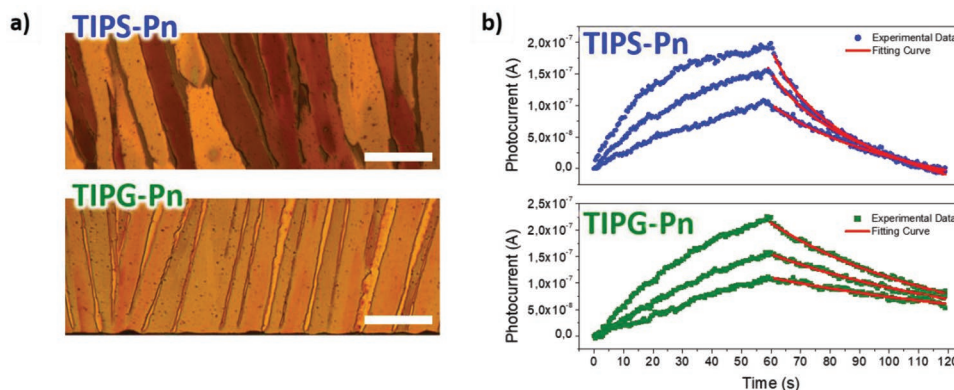


Figure 4. Activation of photoconductive gain mechanism in TIPS-Pn and TIPG-Pn. a) Optical images of the TIPS-Pn and TIPG-Pn layers deposited at 0.6 and 0.4 mm s⁻¹, respectively. These films present similar morphologies. Scale bar = 20 μm . b) Dynamical curves of the X-ray detection responses for both the devices when the system has been irradiated for 60 s at three different dose rates: [3.4, 6.0, 8.6] mGy s⁻¹. According to the photoconductive gain model, the discharge of the curves is fitted by a stretched exponential from which it is possible to extract the parameters that determine τ_R , τ_T , and G.

Table 1. Properties of TIPS-Pn and TIPG-Pn-based devices. The mobility and the sensitivity values are obtained as the average over six OFETs fabricated following the same procedures. The recombination time τ_r has been calculated considering the maximum tested dose rate (8.6 mGy s^{-1}). The attenuated fraction is calculated for the two different molecules and thicknesses using the tabulated data reported by NIST for energy 15.2 keV .^[45]

	Dep. speed [mm s^{-1}]	Thickness [nm]	μ [$\text{cm}^2 \text{V}^{-1} \text{s}^{-1}$]	Sensitivity [$\mu\text{C Gy}^{-1} \text{cm}^{-3}$]	τ_r [s]	τ_T [s]	G	Att. fraction [%]
TIPS-Pn	0.6	150 ± 20	0.10 ± 0.02	$(3.0 \pm 0.5) \times 10^7$	200	8×10^{-6}	25×10^6	0.002
TIPG-Pn	0.4	80 ± 30	0.12 ± 0.01	$(9 \pm 2) \times 10^7$	100	7×10^{-6}	14×10^6	0.013

the lower-than-expected TIPG-Pn sensitivity, we further investigated the amplification mechanism governing the ionizing radiation detection in organic thin film-based devices. The samples chosen for this comparison allow us to exclude effects due to the charge collecting properties (which are comparable for the two devices) focusing only on the different activation of PG due to the different efficacy of the minority carrier trap states. According to the PG model, the discharge of the curves reported in Figure 4b

can be fitted using a stretched exponential (i.e., $\rho_x = \rho_0 e^{-\frac{t}{\tau}}^\alpha$) to extract the parameters which determine the characteristic times τ_r and τ_T . More details about the kinetic model and the fitting procedure are reported in previous work by Basiricò et al.^[17] The values reported in Table 1 clearly show that while the transit time for the two devices is comparable, the recombination time of the TIPS-Pn-based OFET is two times higher than that of the TIPG-Pn. This difference leads to a higher gain factor registered for TIPS-Pn detectors, suggesting that the activation of the PG is more effective in the silicon-based molecule than in the germanium-based one. Hence, the lower-than-expected TIPG-Pn sensitivity can be quantitatively justified considering both the different attenuation fractions and the different simulated gain factors for the two molecules. In the range of doses employed to test the detectors, where the X-ray-induced photocurrent is linearly dependent on the dose rates, the discrepancy between the two experimental sensitivity values is quantitatively demonstrated by the following equivalence

$$\frac{S_{\text{TIPG}}}{S_{\text{TIPS}}} = \frac{G_{\text{TIPG}} \times I_{\text{CC-TIPG}}}{G_{\text{TIPS}} \times I_{\text{CC-TIPS}}} \quad (2)$$

where S_{TIPS} and S_{TIPG} are the sensitivity values experimentally measured, respectively, for TIPS-Pn and TIPG-Pn-based detectors, G_{TIPS} and G_{TIPG} are the gain factors simulated, respectively, for TIPS-Pn and TIPG-Pn-based detectors, and $I_{\text{CC-TIPS}}$ and $I_{\text{CC-TIPG}}$ are the photocurrents directly generated by the absorption of high energy photons and directly related to the X-ray absorption fraction ($I_{\text{CC}} = q \Phi n$, where q is the elementary charge, Φ is the photon absorption rate, n is the number of the generated electron-hole pairs per absorbed photon).

Here, we assumed analog values of electron-hole pairs generated per absorbed photon in the two active materials because of their comparable energy gap ($(1.60 \pm 0.03) \text{ eV}$ for TIPG-Pn and $(1.56 \pm 0.09) \text{ eV}$ for TIPS-Pn^[20]) and thus, the ratio between the two I_{CC} results equal to the ratio between the two attenuated fractions reported in Table 1.

To further investigate the origin of the differences in activation of the PG in TIPS-Pn and TIPG-Pn-based detectors, we carried out photocurrent spectroscopy optical quenching experiments (Figure 5). We exposed the OFETs shown in Figure 4 to

X-rays under three different conditions as detailed in Figure 5a: i) in dark; ii) illuminated by a light emitting diode (LEDs) at $\lambda = 450 \text{ nm}$; and iii) illuminated by LED at $\lambda = 855 \text{ nm}$ with the same photon flux ($2.3 \times 10^{13} \text{ photons s}^{-1} \text{ cm}^{-2}$). We selected these wavelengths for two reasons: 1) they allow us to investigate different regions of the photocurrent (PC) spectrum, since 450 nm is above band-gap and 855 nm is below band-gap in both materials ($E_{\text{G-TIPG-Pn}} = 1.67 \pm 0.08 \text{ eV}$; $E_{\text{G-TIPS-Pn}} = 1.62 \pm 0.06 \text{ eV}$); 2) TIPS-Pn and TIPG-Pn PC spectra show (Figure 5b) the most relevant difference in the wavelength range $300\text{--}500 \text{ nm}$. Two excitonic peaks ($\lambda = 370 \text{ nm}$ and $\lambda = 440 \text{ nm}$) are present in both the materials but with a higher intensity in TIPS-Pn.

Figure 5c shows the effects of LED illumination on the X-ray signals. The dynamic curves are acquired under a constant visible illumination while switching the X-ray beam on/off, and they have been normalized to the maximum photocurrent recorded in the dark for both molecules. Illuminating the samples with the 855 nm LED does not induce relevant changes in the radiation detection response and the small reduction of the signal can be attributed to the stress of the sensor induced by the continuous polarization and the multiple irradiation cycles. Conversely, illumination under 450 nm light provokes the total quenching of the X-ray detection response for both molecules, and when the X-rays are turned on, a dramatic decrease of the I_{DS} is recorded. We hypothesize that this effect can be ascribed to interference between the two PG mechanisms impacting visible light^[46] and X-ray detection in organic polycrystalline thin films. The density of trap states for minority carriers can tune the inner amplification of the photocurrent and it strongly affects the detection of both ionizing radiation^[25] and visible light.^[47,48]

Several works in the literature report different strategies adopted to tune the density of traps in organic semiconductor-based devices. Specifically, by varying the density of grain boundaries, the semiconductor/dielectric interfaces, and/or the semiconductor/metal interfaces, it is possible to induce traps for minority carriers and amplify the sensitivity of visible light and X-ray detection. Kymissis et al. reported a study^[47] concerning the role of excitonic states in the photodetection of pentacene-based OFETs. They observed that electron traps selectively induced at the dielectric/semiconductor interface enhance the photoconductivity of the transistors, under λ in the same range studied in this work ($350\text{--}480 \text{ nm}$). Jurchescu et al.^[48] conducted a study on diF-TES-ADT-based OFETs and they measured the number of photocharges induced by UV-vis illumination (in the range $450\text{--}600 \text{ nm}$). They correlated the PG amplification for photon energies above the band-gap to exciton creation and electron trapping, which induces a lowering of the potential barrier and enhances majority carrier injection. Our

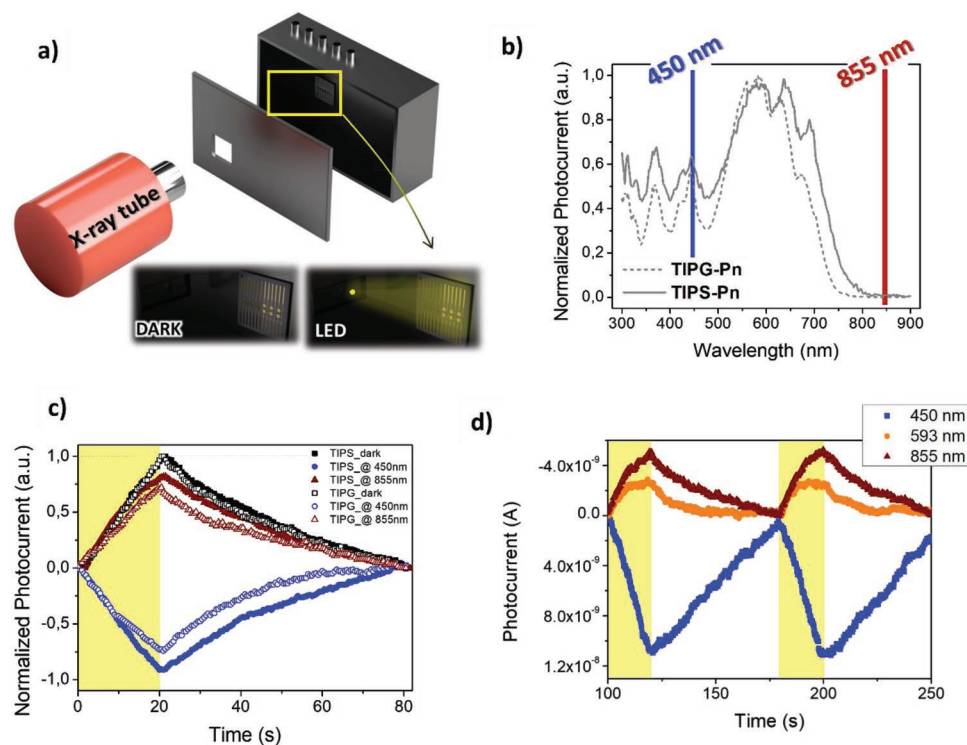


Figure 5. Photoconductive gain effect and active trap states. a) Experimental setup for the investigation of the role played by active trap states in terms of PG effect (i.e., detection response). The OFETs were irradiated by X-rays in the dark and while illuminated by two different LEDs (450 and 855 nm) with the same photon flux (2.3×10^{13} photons $s^{-1} cm^{-2}$). b) Photocurrent spectra for TIPS-Pn (solid) and TIPG-Pn (dotted) normalized with respect to the maximum. c) Dynamic response under X-ray irradiation (yellow shadow) of the TIPS-Pn and TIPG-Pn-based detectors (solid and open symbols, respectively) in the dark (black), and while constantly illuminated with 855 nm (red) and 450 nm (blue) light (2.3×10^{13} photons $s^{-1} cm^{-2}$). For both molecules, the dynamic curves acquired under the three different conditions are normalized to the one acquired in the dark. The samples were irradiated by a tungsten target X-ray tube kept at 40 kVp, dose rate of 8.6 mGy s^{-1} , the OFETs were biased at $V_{DS} = -20$ V; $V_{GS} = -5$. d) Photocurrent induced in the TIPS-Pn-based detector by X-rays while constantly illuminated with 855 nm (red), 593 nm (orange), and 450 nm (blue) light (2.3×10^{13} photons $s^{-1} cm^{-2}$). The sample was irradiated by a tungsten target X-ray tube kept at 40 kVp, dose rate of 8.6 mGy s^{-1} , the OFETs were biased at $V_{DS} = -20$ V; $V_{GS} = -5$.

measurements (Figure 5c) suggest that the observed quenching of the X-ray-induced photocurrent (I_{DS}) under 450 nm light can be ascribed to the presence of traps for minority carriers. Constant illumination with visible photons above the band-gap energy range and at specific excitonic λ is likely to fill and saturate electron traps which become electrically inactive and quench the PG (G factor) related to X-ray detection. Additionally, the filled electron traps may start to behave as recombination centers inducing a reduction of the total current.

This interpretation would further explain the lower G factor and the poorer efficacy of the PG effect in the TIPG-Pn-based detectors compared to TIPS-Pn. In fact, the decrease of I_{DS} measured for TIPS-Pn OFETs exposed to 450 nm is more substantial than the one observed for TIPG-Pn (Figure 5c). Further, the excitonic peak at 450 nm in the photocurrent spectra is higher for TIPS-Pn than for TIPG-Pn (Figure 5b). These two aspects suggest the lower density of electron traps able to activate the PG in the Ge-based molecule, and that justifies the lower than expected sensitivity values measured for TIPG-Pn detectors.

Figure 5d compares the effects of illuminating with different wavelengths (593 nm, above band gap and 855 nm below the band gap), both outside the range reported by Kymissis et al.,^[47] and simultaneously with X-rays. By these measurements, we see the effective activation of PG induced by high energy

photons. Only a small degradation of the photocurrent could be observed when illuminating with the 593 nm LED due to the absorption of visible photons above band gap, correlated to a large conductivity increase and a decrease in the X-ray signal-to-noise ratio. The interference of the two phenomena induced by X-ray and visible light illumination is only present under 450 nm illumination and strongly suggests that the electron traps at this specific energy play a crucial role in the activation of the PG mechanism.

3. Conclusion

In this work, we report high-performance flexible X-ray detectors based on organic thin-film field effect transistors. The organic active layer is either a TIPS-Pn or a TIPG-Pn thin film deposited from solution by a PNP technique, which allows full control of the crystallization of the thin films over large areas. The tuning of the morphology and packing of the polycrystalline structures permit control over the minority and majority carrier trap states, which regulate the PG mechanism. By an effective enhancement of the thin-film transport properties and of the efficiency of the electron traps controlling the PG effect, we reached a record X-ray sensitivity value among

flexible radiation detectors $S = (9.0 \pm 0.4) \times 10^7 \mu\text{C Gy}^{-1} \text{cm}^{-3}$. We further investigated the role played by trap states in the activation of the PG by photocurrent spectroscopy optical quenching experiments. By comparing the activation of electrically active minority carrier traps induced by the simultaneous irradiation with X-rays and visible light, we experimentally identified for the first time the excitonic peaks which mediate the PG effect, and we could evaluate the different efficiencies of the inner amplification mechanism activation in TIPS-Pn and TIPG-Pn-based thin-film X-ray detectors.

4. Experimental Section

Device Fabrication: The devices were fabricated onto PEN substrate 125 μm thick. The gate electrode was formed by chromium (5 nm thick) and gold (60 nm thick) deposited by electron beam evaporation. The dielectric was formed by 200 nm of parylene C deposited by chemical vapor deposition. The source and drain electrodes were formed by gold (60 nm thick) deposited by electron beam and they presented an interdigitated geometry ($L = 40 \mu\text{m}$ and $W = 30\text{--}40 \text{nm}$) to maximize the channel width keeping a limited pixel area ($A = 4 \text{mm}^2$). Before the printing of the organic semiconducting layer, the source and drain electrodes were functionalized with a self-assembled monolayer of 2,3,4,5,6-pentafluorobenzenethiol (PBFT) to improve the injection/extraction of charges from the organic semiconducting layer and crystallinity of the contact.^[49] At the end of the fabrication process, after the printing of the organic materials, an annealing at 90 °C for 1 h took place to let evaporate any solvent residual.

PNP Procedure: The syringe connected to a pressure controller and the needle (500 μm in diameter) were employed for the solution reservoir and the printing nozzle, respectively. The samples were placed on a holder heated and kept at 50 °C during all the printing procedure. Both the syringe and the sample holder were interfaced with a 3D stage to control the position and the printing motion. Both TIPS-Pn and TIPG-Pn were prepared in solution with anhydrous toluene at a concentration of 15 mg mL⁻¹.

Electrical Characterization: OFET electrical performance was measured using a Keithley 2614 SourceMeter, controlled by a custom made Labview software, at ambient conditions. The field-effect mobility (μ) and threshold voltage (V_{th}) were extracted in the saturation regime from a linear fit of the plot (I_{DS})^{1/2} versus V_{GS} . Mobility was extracted using the relationship

$$\mu = \frac{\left(\frac{\partial \sqrt{I_{DS}}}{\partial V_{GS}}\right)^2}{\frac{1}{2} \frac{W}{L} C} \quad (3)$$

where C is the insulator capacitance per unit area, and W and L are the channel width and length, respectively. The subthreshold swing slope S was calculated using the following equation

$$S = \left(\frac{\partial \log I_{DS}}{\partial V_{GS}}\right) \Big|_{I_{max}}^{-1} \quad (4)$$

X-Ray Irradiation: Characterization under X-rays was performed using the X-ray broad spectrum provided by a tungsten tube with an accelerating voltage of 40 kV and tube current of 100, 200, 350 500 μA . These corresponded to dose rates in the range 1.6–8.6 mGy s⁻¹, measured with an error below 5% by means of the arithmetic mean over 10 pulses of the output of a calibrated commercial detector (BARRACUDA X-Ray Analyzer from RTI) in the same position of the sensor under study. The dose rates were expressed in air kerma. The mean photon energy in this irradiation conditions was 15.2 keV. During these measurements, the

samples were kept in dark in a metal Faraday cage to keep the sample in dark and to screen the external electromagnetic noise.

AFM Measurements: AFM measurements were performed on a Park NX10 system using PPP-NCHR tips (Nanosensors) in noncontact mode and applying adaptive scan rate to slow down scan speed at crystallite borders.

Statistical Analysis: The electrical parameters and the X-ray sensitivities were the mean value calculated over six OFETs fabricated in the same conditions. The statistical errors were corresponded to the standard deviation. The photocurrent values induced by each dose rates were the mean value of three subsequent irradiation cycles and the statistical error was the standard deviation.

Supporting Information

Supporting Information is available from the Wiley Online Library or from the author.

Acknowledgements

I.F., L.B., A.C., and B.F. acknowledge funding from INFN through the CSN5 FIRE project. J.E.A. acknowledges funding from the U.S. National Science Foundation's DMREF program (DMR-1627428).

Open access funding provided by Universita degli Studi di Bologna within the CRUI-CARE Agreement.

Conflict of Interest

The authors declare no conflict of interest.

Data Availability Statement

The data that support the findings of this study are available from the corresponding author upon reasonable request.

Keywords

flexible electronics, organic direct X-ray detectors, organic thin-film transistors, photoconductive gain, printing

Received: May 11, 2022
Revised: September 2, 2022
Published online: October 25, 2022

- [1] L. Basiricò, A. Ciavatti, B. Fraboni, *Adv. Mater. Technol.* **2020**, *6*, 2000475.
- [2] M. J. Griffith, S. Cottam, J. Stamenkovic, J. A. Posar, M. Petasecca, *Front. Phys.* **2020**, *8*, 22.
- [3] L. Basiricò, A. Ciavatti, I. Fratelli, D. Dreossi, G. Tromba, S. Lai, P. Cosseddu, A. Bonfiglio, F. Mariotti, C. Dalla Val, V. Bellucci, J. E. Anthony, B. Fraboni, *Front. Phys.* **2020**, *8*, 13.
- [4] A. M. Zeidell, T. Ren, D. S. Filston, H. F. Iqbal, E. Holland, J. D. Bourland, J. E. Anthony, O. D. Jurchescu, *Adv. Sci.* **2020**, *7*, 2001522.
- [5] I. Fratelli, A. Ciavatti, E. Zanazzi, L. Basiricò, M. Chiari, L. Fabbri, J. E. Anthony, A. Quaranta, B. Fraboni, *Sci. Adv.* **2021**, *7*, eabf4462.
- [6] A. Intaniwet, C. A. Mills, M. Shkunov, P. J. Sellin, J. L. Keddie, *Nanotechnology* **2012**, *23*, 235502.

- [7] A. Ciavatti, T. Cramer, M. Carroli, L. Basiricò, R. Fuhrer, D. M. De Leeuw, B. Fraboni, *Appl. Phys. Lett.* **2017**, *111*, 183301.
- [8] H. M. Thirimanne, K. D. G. I. Jayawardena, A. J. Parnell, R. M. I. Bandara, A. Karalasingam, S. Pani, J. E. Huerdler, D. G. Lidzey, S. F. Tedde, A. Nisbet, C. A. Mills, S. R. P. Silva, *Nat. Commun.* **2018**, *9*, 2926.
- [9] H. F. Haneef, A. M. Zeidell, O. D. Jurchescu, *J. Mater. Chem. C* **2020**, *8*, 759.
- [10] S. Yang, S. Park, J. Binting, Y. Bonnassieux, J. Anthony, I. Kyriassis, *Adv. Electron. Mater.* **2018**, *4*, 1700534.
- [11] M. Singh, H. M. Haverinen, P. Dhagat, G. E. Jabbour, *Adv. Mater.* **2010**, *22*, 673.
- [12] I. Temiño, F. G. Del Pozo, M. R. Ajayakumar, S. Galindo, J. Puigdollers, M. Mas-Torrent, *Adv. Mater. Technol.* **2016**, *1*, 1600090.
- [13] J. C. Sorli, Q. Ai, D. B. Granger, K. Gu, S. Parkin, K. Jarolimek, N. Telesz, J. E. Anthony, C. Risko, Y. L. Loo, *Chem. Mater.* **2019**, *31*, 6615.
- [14] H. Ling, S. Liu, Z. Zheng, F. Yan, *Small Methods* **2018**, *2*, 1800070.
- [15] R. Janneck, F. Vercesi, P. Heremans, J. Genoe, C. Rolin, *Adv. Mater.* **2016**, *28*, 8007.
- [16] G. Giri, E. Verploegen, S. C. B. Mannsfeld, S. Atahan-Evrenk, D. H. Kim, S. Y. Lee, H. A. Becerril, A. Aspuru-Guzik, M. F. Toney, Z. Bao, *Nature* **2011**, *480*, 504.
- [17] L. Basiricò, A. Ciavatti, T. Cramer, P. Cosseddu, A. Bonfiglio, B. Fraboni, *Nat. Commun.* **2016**, *7*, 13063.
- [18] C. S. Lien *Physics of Optoelectronic Devices*, John Wiley & Sons Inc., Hoboken, NJ **1995**.
- [19] S. Lai, P. Cosseddu, L. Basiricò, A. Ciavatti, B. Fraboni, A. Bonfiglio, *Adv. Electron. Mater.* **2017**, *3*, 1600409.
- [20] A. Ciavatti, L. Basiricò, I. Fratelli, S. Lai, P. Cosseddu, A. Bonfiglio, J. E. Anthony, B. Fraboni, *Adv. Funct. Mater.* **2018**, *29*, 1806119.
- [21] J. E. Anthony, D. L. Eaton, S. R. Parkin, *Org. Lett.* **2002**, *4*, 15.
- [22] A. J. Petty, Q. Ai, J. C. Sorli, H. F. Haneef, G. E. Purdum, A. Boehm, D. B. Granger, K. Gu, C. P. L. Rubinger, S. R. Parkin, K. R. Graham, O. D. Jurchescu, Y. L. Loo, C. Risko, J. E. Anthony, *Chem. Sci.* **2019**, *10*, 10543.
- [23] J. E. Anthony, *Chem. Rev.* **2006**, *106*, 5028.
- [24] J. E. Anthony, J. S. Brooks, D. L. Eaton, S. R. Parkin, *J. Am. Chem. Soc.* **2001**, *123*, 45.
- [25] I. Temiño, L. Basiricò, I. Fratelli, A. Tamayo, A. Ciavatti, M. Mas-Torrent, B. Fraboni, *Nat. Commun.* **2020**, *11*, 2136.
- [26] A. Tamayo, I. Fratelli, A. Ciavatti, C. Martínez-Domingo, P. Branchini, E. Colantoni, S. De Rosa, L. Tortora, A. Contillo, R. Santiago, S. T. Bromley, B. Fraboni, M. Mas-Torrent, L. Basiricò, *Adv. Electron. Mater.* **2022**, <https://doi.org/10.1002/aem.202200293>.
- [27] Y. Gao, Y. Ge, X. Wang, J. Liu, W. Liu, Y. Cao, K. Gu, Z. Guo, Y.-M. Wei, N. Zhou, D. Yu, H. Meng, X.-F. Yu, H. Zheng, W. Huang, J. Li, *Adv. Mater.* **2021**, *33*, 2101717.
- [28] M. P. A. Nanayakkara, L. Matjačić, S. Wood, F. Richeimer, F. A. Castro, S. Jenatsch, S. Züfle, R. Kilbride, A. J. Parnell, M. G. Masteghin, H. M. Thirimanne, A. Nisbet, K. D. G. I. Jayawardena, S. R. P. Silva, *Adv. Funct. Mater.* **2020**, *31*, 2008482.
- [29] M. P. A. Nanayakkara, M. G. Masteghin, L. Basiricò, I. Fratelli, A. Ciavatti, R. C. Kilbride, S. Jenatsch, T. Webb, F. Richeimer, S. Wood, F. A. Castro, A. J. Parnell, B. Fraboni, K. D. G. I. Jayawardena, S. R. P. Silva, *Adv. Sci.* **2021**, *9*, 2101746.
- [30] H. M. Thirimanne, K. D. G. I. Jayawardena, A. Nisbet, Y. Shen, R. M. I. Bandara, C. A. Mills, G. Shao, S. R. P. Silva, *IEEE Trans. Nucl. Sci.* **2020**, *67*, 2238.
- [31] K. D. G. I. Jayawardena, H. M. Thirimanne, S. F. Tedde, J. E. Huerdler, A. J. Parnell, R. M. I. Bandara, C. A. Mills, S. R. P. Silva, *ACS Nano* **2019**, *13*, 6973.
- [32] P. Zhao, J. Su, Y. Guo, L. Wang, Z. Lin, J. Zhang, Y. Hao, X. Ouyang, J. Chang, *Mater. Today Phys.* **2021**, *20*, 100446.
- [33] B. Shabbir, J. Liu, V. Krishnamurthi, R. A. W. Ayyubi, K. Tran, S. A. Tawfik, M. M. Hossain, H. Khan, Y. Wu, B. N. Shivananju, R. U. R. Sagar, A. Mahmood, A. Younis, M. H. Uddin, S. A. Bukhari, S. Walia, Y. Li, M. J. S. Spencer, N. Mahmood, J. J. Jasieniak, *Adv. Funct. Mater.* **2022**, *32*, 2105038.
- [34] H. Li, X. Shan, J. N. Neu, T. Geske, M. Davis, P. Mao, K. Xiao, T. Siegrist, Z. Yu, *J. Mater. Chem. C* **2018**, *6*, 11961.
- [35] H. Mescher, F. Schackmar, H. Eggers, T. Abzieher, M. Zuber, E. Hamann, T. Baumbach, B. S. Richards, G. Hernandez-Sosa, U. W. Paetzold, U. Lemmer, *ACS Appl. Mater. Interfaces* **2020**, *12*, 15774.
- [36] H. Tsai, F. Liu, S. Shrestha, K. Fernando, S. Tretiak, B. Scott, D. T. Vo, J. Strzalka, W. Nie, *Sci. Adv.* **2020**, *6*, eaay0815.
- [37] J. Zhao, L. Zhao, Y. Deng, X. Xiao, Z. Ni, S. Xu, J. Huang, *Nat. Photonics* **2020**, *14*, 612.
- [38] J. Liu, B. Shabbir, C. Wang, T. Wan, Q. Ou, P. Yu, A. Tadich, X. Jiao, D. Chu, D. Qi, D. Li, R. Kan, Y. Huang, Y. Dong, J. Jasieniak, Y. Zhang, Q. Bao, *Adv. Mater.* **2019**, *31*, 1901644.
- [39] A. Ciavatti, R. Sorrentino, L. Basiricò, B. Passarella, M. Caironi, A. Petrozza, B. Fraboni, *Adv. Funct. Mater.* **2021**, *31*, 2009072.
- [40] J. Guo, Y. Xu, W. Yang, B. Xiao, Q. Sun, X. Zhang, B. Zhang, M. Zhu, W. Jie, *ACS Appl. Mater. Interfaces* **2021**, *13*, 23928.
- [41] S. Demchyshyn, M. Verdi, L. Basiricò, A. Ciavatti, B. Hailegnaw, D. Cavalcoli, M. C. Scharber, N. S. Sariciftci, M. Kaltenbrunner, B. Fraboni, *Adv. Sci.* **2020**, *7*, 2002586.
- [42] L. Basiricò, S. P. Senanayak, A. Ciavatti, M. Abdi-Jalebi, B. Fraboni, H. Sirringhaus, *Adv. Funct. Mater.* **2019**, *29*, 1902346.
- [43] H. Han, S. Lee, J. Seo, C. Mahata, S. H. Cho, A. R. Han, K. S. Hong, J. H. Park, M. J. Soh, C. Park, T. Lee, *Nanoscale Res. Lett.* **2014**, *9*, 610.
- [44] L. Mao, Y. Li, H. Chen, L. Yu, J. Zhang, *Nanomaterials* **2021**, *11*, 20.
- [45] NIST – X-ray Mass Attenuation Coefficients, <https://doi.org/10.18434/T4D01F>.
- [46] K.-J. Baeg, M. Binda, D. Natali, M. Caironi, Y.-Y. Noh, *Adv. Mater.* **2013**, *25*, 4267.
- [47] Z. Jia, L. Banu, I. Kyriassis, *IEEE Trans. Electron Devices* **2010**, *57*, 380.
- [48] Z. Jagoo, Z. A. Lamport, O. D. Jurchescu, L. E. McNeil, *Appl. Phys. Lett.* **2021**, *119*, 073302.
- [49] C.-H. Kim, H. Hlaing, M. M. Payne, K. G. Yager, Y. Bonnassieux, G. Horowitz, J. E. Anthony, I. Kyriassis, *ChemPhysChem* **2014**, *15*, 2913.